TMTT-2022-07-0982.R1

Oscillators based on Step-Impedance and Slow-Wave Transmission Lines for Sensing Applications

Mabel Pontón, *Member*, *IEEE*, Sergio Sancho, *Member*, *IEEE*, Amparo Herrera, and Almudena Suárez, *Fellow*, *IEEE*

***Abstract*— This work investigates the capabilities of oscillators based on step-impedance and slow-wave structures to sense dielectric constants. The material under test (MUT) is placed over the structure and the objective is to achieve a high sensitivity of the oscillation frequency with the advantage of a low phase noise, enabled by the high-quality factor of the structure. With the aid of simplified analytical models, we will initially study the variation of the resonance frequency of a step-impedance transmission line with the dielectric constant of the MUT, paying attention to the influence of the number of line sections. The study includes the derivation of analytical expressions for the sensitivity of the resonance frequency. Next the structure will be connected to the oscillator active core, which will be modeled with a numerical nonlinear admittance function extracted from harmonic-balance (HB) simulations. The resulting semi-analytical formulation will provide insight into the variation of the oscillation frequency and amplitude with the dielectric constant of the MUT, as well as the variation of the phase-noise spectral density. It will also enable a versatile test and optimization of the various structures to achieve a high sensitivity with a low phase noise. The methods have been successfully applied to a FET-based oscillator at about 2 GHz.**

***Index Terms*—Slow-wave structure, oscillator, bifurcation.**

I. Introduction

MICROWAVE sensors are very sensitive to the material properties, have a low cost and are compatible with planar fabrication processes [1]-[8]. A common sensing mechanism is the variation of the resonance frequency of a passive structure [1]-[4] in the presence of the material under test (MUT). Some examples are the works [1]-[2], which make use of step-impedance resonators and [3]-[4], which make use of split ring resonators [3]-[4]. On the other hand, the recent works [5]-[9] are based on the detection of phase variations [10]-[12] when exciting the system at a constant frequency. In those sensors, which operate in either transmission or reflection mode, the phase varies in the presence of the MUT. Implementations based on meandered lines [5], open-ended step-impedance lines [6]-[7], and slow-wave structures [8]-[9] have been demonstrated, analyzing, in each case, the phase sensitivity to the MUT dielectric constant. The dielectric covers at least a part of these structures and very good results are obtained in transmission mode, for slow-wave structures [8]-[9], and reflection mode, for open-ended step impedance lines [6]-[7]. On the other hand, the work [13] presents a detailed analysis of oscillators containing a slow-wave structure [14]-[18], which enables a low phase-noise spectral density. In fact, oscillator-based sensors [19]-[29] have the advantage of a self-sustained operation, in which the MUT variations give rise to a change in the oscillation amplitude and frequency [21]-[22], easily measured with the aid of amplitude or frequency detection interfaces; for instance, frequency variations can be detected from the control voltage of a synthesizer and amplitude variations by means of a power detector or through the control voltage of a feedback loop [10],[21],[25]-[28].

In oscillator sensors, the accuracy will be degraded by the phase noise, which will affect the measurement reliability and repeatability. Using a passive structure with a high frequency selectivity, the oscillator will both exhibit a low phase noise and be able to track the variation of the structure resonance frequency with the MUT dielectric constant. Thus, this work extends [13] with the investigation of the possible use of oscillators based on step-impedance transmission lines [6]-[7] or on slow-wave structures [8]-[9], [14]-[18] to implement low-cost dielectric sensors. Emphasis will be placed on the standalone oscillator operation since, as stated, frequency and amplitude detection methods have been established in the literature.

As in [5]-[9], the material to be sensed will be placed over the step-impedance or slow-wave structure. In the investigation presented here, it will cover the entire structure, though it would be possible to particularize the study to some sections only. With the aid of simplified analytical models, we will initially study the variation of the resonance frequency of a step-impedance transmission line with the dielectric constant of the MUT, paying attention to the influence of the number of line sections, as well as the structure geometry. The study includes the derivation of analytical expressions for the sensitivity of the resonance frequency to the MUT dielectric constant, defined

Manuscript received July 8, 2022; revised September 26, 2022. This work was supported by the Spanish Ministry of Science and Innovation (MCIN/ AEI /10.13039/501100011033) under grant PID2020-116569RB-C31.This article is an expanded version from the IEEE MTT-S International Microwave Symposium (IMS 2022), Denver, CO, USA, June 19-24, 2022. (*Corresponding author*: *Mabel Pontón*).

The authors are with the Departamento de Ingeniería de Comunicaciones, Universidad de Cantabria, Santander, 39005, Spain (e-mail: mabel.ponton@unican.es; sanchosm@unican.es; herreraa@unican.es; suareza@unican.es).

here as the derivative of this resonance frequency with respect to the dielectric constant. Then the structure will be connected to the oscillator active core, which will be modeled with a numerical nonlinear admittance function extracted from harmonic-balance (HB) simulations [13], [30]. This nonlinear admittance will be combined with the passive linear one of each sensing structure, initially described in an analytical manner. This formulation disregards the impact of the structure at the second and higher harmonic terms. Provided the harmonic content is low at the analysis node, it will constitute a valid approach, as will be demonstrated through a rigorous comparison with harmonic balance (HB) considering multiple harmonic terms. The various sensing structures will be introduced at the same node of the oscillator active core, so the nonlinear admittance function will be the same in all cases. The phase-noise spectral density will be calculated through a perturbation analysis of the semi-analytical formulation.

The presented semi-analytical formulation provides insight into the variation of the oscillation frequency and amplitude with the dielectric constant, as well as the oscillator capability to track the resonance frequency; it also clarifies the mechanism for the oscillation extinction and the impact of losses. Although step-impedance transmission lines of the kind in [6]-[7] and slow-wave structures have been considered, the main conclusions and analysis methodologies should be applicable when basing the oscillator on other resonators.

All the tests will be carried out on a transistor-based oscillator, operating at about 2 GHz. The practical design will rely on a realistic description of the sensing structures using multi-layer models [31]. In these conditions, the full oscillator circuit will be analyzed through a separate extraction of the nonlinear and linear admittance functions describing the active core and the sensing structures, respectively. These functions will be combined in a steady-state oscillation equation, solved through a contour-intersection procedure [32]. This will enable a straight-forward tracing of the solution curves, including any possibly multi-valued sections. Comparisons with results based on electromagnetic simulations of the planar structures, fully compatible with these novel analysis methods, will also be carried out. Several prototypes have been manufactured and measured, obtaining a very good agreement with the analysis results.

The manuscript is organized as follows. Section II presents the analysis the step-impedance transmission lines and the sensitivity of their resonance frequencies to the MUT dielectric constant. Section III describes the oscillator behavior, focusing on the sensitivity of the oscillation frequency to the dielectric constant and the phase-noise spectral density. Section IV presents the practical design, which considers both a step-impedance transmission line and a slow-wave structure; it includes electromagnetic simulations and measurements.

II. Resonance Analysis of the Planar Structures

The oscillator will be analyzed in terms of admittance functions, so each structure will be described with its passive-linear input admittance Y_{in}, calculated between the node to be connected to the oscillator and ground (Fig. 1). Note that this admittance will depend on the excitation frequency and the unknown dielectric constant ε_{mut} of the MUT, which will be placed over the structure, as in [5]-[9]. In the following derivation we will assume that the MUT covers the whole structure, though the formulation can be particularized to some sections only.

As shown in Fig. 1, we will initially consider the cases of an ordinary λ/2 resonator and several open-ended step-impedance lines with an even and odd number of sections, synthesized to obtain the same resonance frequency (2.4 GHz) in the absence of the MUT. Note that the electrical length of the final section will be different for an odd number of stages and for an even number (Fig. 1).

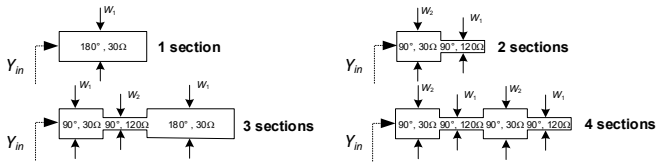

Fig. 1. Step-impendence transmission lines considered in the semi-analytical investigation.

A. Input admittance

The open-ended step-impedance transmission lines have the same structure considered in the practical implementations of [6]-[7], though here the goal will be to predict the variation of their resonance frequencies with ε_{mut} (instead of the phase-shift of their reflection coefficient). The electrical lengths, ϕ_{oi}, will be calculated at a given reference frequency f_{ro}. In the absence of the MUT, for an odd number of stages, the electrical length of the most external section will be $\phi_1 = \phi_{o1} = \pi$, with a high characteristic admittance Y_{o1}; in turn, for an even number of stages, the electrical length of the most external section will be $\phi_1 = \phi_{o1} = \pi/2$, with a low Y_{o1}. In the two cases, the rest of electrical lengths (for $i > 1$) will be $\phi_{oi} = \pi/2$, with alternating low and high characteristic admittances Y_{oi}. For each number n of transmission-line sections, the corresponding input admittance $Y_{in,n}$ (required for the oscillator analysis of Section III) is obtained from the following recursive expression:

$$Y_{in1} = jY_{o1}\tan\phi_1,$$
$$Y_{in,n} = Y_{o,n}\frac{Y_{in,n-1} + jY_{o,n}\tan\phi_n}{Y_{o,n} + jY_{in,n-1}\tan\phi_n} \quad (1)$$

Note that the above analytical model neglects losses, so all the above functions are purely imaginary. The physical lengths of the transmission line sections are calculated from:

$$l_i = c\frac{\phi_{oi}}{\omega_{ro}\sqrt{\varepsilon_{eff}(W_i/h)}} \quad (2)$$

where $\omega_{ro} = 2\pi f_{ro}$ and $\varepsilon_{eff}(W_i/h)$ is the effective dielectric constant of the i^{th} section, having a line width W_i and dielectric height h in the absence of the MUT ($\varepsilon_{mut} = 1$). When a material with the dielectric constant ε_{mut} covers the i^{th} section of the planar structure, its effective dielectric constant can be approached with [33]-[34]:

$$\varepsilon_{eff}(\varepsilon_{mut},W_i/h)=\frac{1-F_i}{2}\varepsilon_{mut}+\frac{1+F_i}{2}\varepsilon_r,$$

$$F_i=\begin{cases}(1+12\,h/W_i)^{-1/2}, & h/W_i\le 1\\ (1+12\,h/W_i)^{-1/2}+0.04(1-W_i/h)^2, & h/W_i\ge 1\end{cases} \tag{3}$$

where zero metal thickness and a sufficiently large (ideally infinite) height of the dielectric ε_{mut} are assumed. As shown above, F_i is a geometric factor that depends on the ratio W_i/h between the host microstrip width and substrate height. It increases with W_i/h and varies between 0.04 and 1. Note that $\varepsilon_{eff}(W_i/h)$ in (2) is a particular case of (3) with $\varepsilon_{mut}=1$. In the presence of the MUT, the electrical lengths of the line sections at a given frequency ω are:

$$\phi_i(\omega,\varepsilon_{mut})=\frac{\omega}{c}l_i\sqrt{\varepsilon_{eff}(\varepsilon_{mut},W_i/h)}=\phi_{oi}\frac{\omega}{\omega_{ro}}\sqrt{\frac{\varepsilon_{eff}(\varepsilon_{mut},W_i/h)}{\varepsilon_{eff}(W_i/h)}} \tag{4}$$

which for fixed l_i and W_i will depend on both the excitation frequency ω and ε_{mut}. Because the host substrate height is the same for all the transmission-line sections, we will drop the dependence on h. In the presence of the MUT, the characteristic admittances Y_{oi} will also vary. Note that they also depend on W_i/h [35]. They can be expressed as:

$$Y_{oi}(\varepsilon_{mut},W_i)=Y_{oi}(1,W_i)\sqrt{\varepsilon_{eff}(\varepsilon_{mut},W_i)/\varepsilon_{eff}(W_i)} \tag{5}$$

where $Y_{oi}(1,W_i)$ is the characteristic admittance for $\varepsilon_{mut}=1$. As an alternative model, one can use an ordinary microstrip line (without the upper-layer substrate) and artificially modify the value of its dielectric constant to obtain the same effective one $\varepsilon_{eff}(\varepsilon_{mut},W_i/h)$. In the equivalent transmission line, instead of ε_r, we will use $\varepsilon_{r,i}$, which is calculated by equating:

$$\varepsilon_{eff}(\varepsilon_{mut},W_i/h)=\frac{1-F_i}{2}\varepsilon_{mut}+\frac{1+F_i}{2}\varepsilon_r=\frac{1-F_i}{2}1+\frac{1+F_i}{2}\varepsilon_{r,i} \tag{6}$$

where we have assumed $\varepsilon_{mut}=1$ in the second equation, corresponding to an ordinary transmission line. Solving for $\varepsilon_{r,i}$ one obtains:

$$\varepsilon_{r,i}=\frac{(1-F_i)\varepsilon_{mut}+(1+F_i)\varepsilon_r-1+F_i}{1+F_i} \tag{7}$$

In the planar structures of Fig. 1, the reference frequency f_{ro} is 2.4 GHz, so they will all exhibit this resonance frequency for $\varepsilon_{mut}=1$. Fig. 2(a) presents the frequency responses obtained for one (λ/2 resonator), two and three sections under $\varepsilon_{mut}=3$ and 3.1. For $\varepsilon_{mut}=3$, and in the range 1 GHz to 3 GHz, the resonance frequencies (zero crossing with positive slope versus the excitation frequency) for one, two and three sections are 2.23 GHz, 2.11 GHz, and 2.21 GHz, respectively. Note that for each structure there are (ideally) infinite resonance frequencies, and the distance between these frequencies will decrease with the number of line sections. The existence of several resonances in the expected oscillation interval may give rise to undesired oscillation modes, which should be kept in mind at the oscillator-design stage.

With $n=1$, the resonance condition is:

$$\tan\phi_1=0\ \Rightarrow\ \phi_1=\frac{\omega_r(k)}{c}l_1\sqrt{\varepsilon_{eff}(\varepsilon_{mut},W_1/h)}=k\pi,$$

$$\omega_r(k)=\frac{k\pi c}{l_1\sqrt{\varepsilon_{eff}(\varepsilon_{mut},W_1/h)}}=\frac{k\pi c}{l_1\sqrt{\frac{1-F_1}{2}\varepsilon_{mut}+\frac{1+F_1}{2}\varepsilon_r}} \tag{8}$$

For $n=1$, the targeted resonance frequency is the one corresponding to $k=1$. The denominator of (8) is the square root of a straight line in ε_{mut} with the positive slope $(1-F_1)/2$. Thus, the resonance frequency decreases with ε_{mut}. For F_1 close to 1 (a high value of W/h), the first term in the square root will be small, so one can carry out a Taylor series expansion of first order:

$$\omega_r=\frac{\pi c}{l_1\sqrt{\frac{1-F_1}{2}\varepsilon_{mut}+\frac{1+F_1}{2}\varepsilon_r}}\cong\frac{\pi c}{l_1\sqrt{\frac{1+F_1}{2}\varepsilon_r}}-\frac{\pi c}{l_1\left(\frac{1+F_1}{2}\varepsilon_r\right)^{3/2}}\left(\frac{1-F_1}{2}\right)\varepsilon_{mut} \tag{9}$$

The resonance frequency will exhibit a more linear variation for F_1 close to 1, but the sensitivity to ε_{mut} will be smaller. In fact, the sensitivity will increase for a lower F_1; thus, for a narrower transmission line.

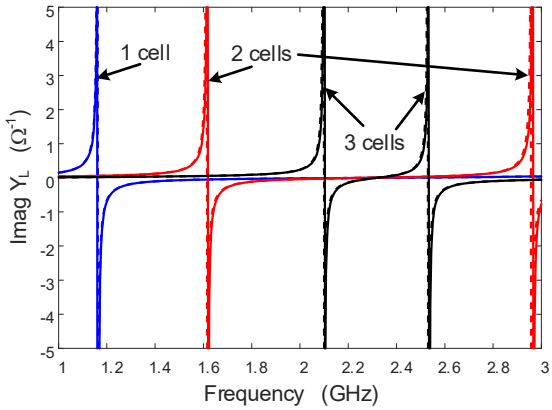

Fig. 2. Frequency responses obtained with one, two and three sections, for $\varepsilon_{mut}=3$ (solid line) and 3.1 (dashed line).

Using the complete expression (9), we have traced the resonance-frequency curve versus ε_{mut}. This curve has been validated with the one obtained through a numerical method that will be very useful under a higher number n of line sections. To obtain the variation of ω_r versus ε_{mut}, we perform a double sweep in ε_{mut} and ω_r and calculate the following zero-value contour:

$$\mathrm{Im}\left[Y_{in,n}(\varepsilon_{mut},\omega_r)\right]=0 \tag{10}$$

In the study performed here, the dielectric constant ε_{mut} has been swept between 1 and 12, and the frequency has been swept in the targeted operation interval, going from 1.4 GHz to 2.4

GHz. The curves resulting for different values of W_1 (and, thus, of F_1) are shown in Fig. 3. The results obtained with the complete analytical expression (9) and with the numerical zero-value contour (10) are overlapped in all cases. In agreement with the previous derivations, the sensitivity increases when reducing F_1.

As the number n of line sections increases, there is a higher complexity in the expression of the input admittance versus both the excitation frequency ω and ε_{mut} [see (1)] Nevertheless, and as shown in the following, the curve ω_r versus ε_{mut} will either exhibit small variations (odd number of sections) or no variation (even number).

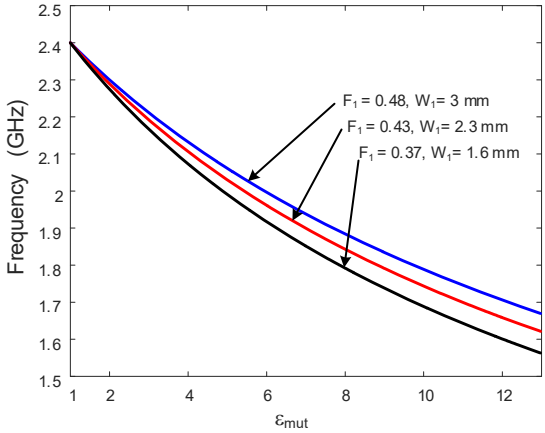

Fig. 3. Case of a λ/2 resonator. Variation of the resonance frequency ω_r versus ε_{mut}. Dependence of F_1. Results obtained with the complete analytical expression (9) and the numerical zero-value contour (10) are overlapped in all cases.

B. Sensitivity of the resonance frequency to ε_{mut}

To facilitate the analysis of the sensitivity of the resonance frequency ω_r to ε_{mut}, we will express the input admittance of the lossless configurations in Fig. 1 in terms of the reflection coefficient $\Gamma = 1e^{j\phi_{ref}(\varepsilon_{mut},\omega_r)}$. At the resonance frequency obtained for each ε_{mut}, we will have:

$$Y_{in,n}(\omega_r) = Y_c \frac{1-\Gamma}{1+\Gamma} = Y_c \frac{1-1e^{j\phi_{ref}(\varepsilon_{mut},\omega_r)}}{1+1e^{j\phi_{ref}(\varepsilon_{mut},\omega_r)}} = 0 \qquad (11)$$

since $\phi_{ref} = 0$. To get some insight into the sensitivity of ω_r with respect to ε_{mut} we will linearize the various structures about $\varepsilon_{mut} = 1$. This linearized analysis is conceptually similar to the one carried out for the phase shift in [7], though here, instead of this phase shift, we are addressing the resonance frequency ω_r. For this analysis, we will consider small increments about the resonance frequency ω_{ro}, at which $\varepsilon_{mut} = 1$ and the electrical lengths have their nominal values ϕ_{oi}. If the increments are small enough to enable the linearization of $Y(\varepsilon_{mut},\omega)$, we will have:

$$\frac{\partial Y_{in,n}(\varepsilon_{mut}=1,\omega_{ro})}{\partial \varepsilon_{mut}}\Delta\varepsilon_{mut} + \frac{\partial Y_{in,n}(\varepsilon_{mut}=1,\omega_{ro})}{\partial \omega}\Delta\omega_r = 0 \qquad (12)$$

And the frequency sensitivity, defined here as the derivative $\partial\omega_r / \partial\varepsilon_{mut}$, can be calculated as:

$$\frac{\partial\omega_r}{\partial\varepsilon_{mut}} = \frac{\Delta\omega_r}{\Delta\varepsilon_{mut}} = -\frac{\dfrac{\partial Y(\varepsilon_{mut}=1,\omega_{ro})}{\partial\varepsilon_{mut}}}{\dfrac{\partial Y(\varepsilon_{mut}=1,\omega_{ro})}{\partial\omega}} \qquad (13)$$

Applying the chain rule:

$$\frac{\partial Y(\omega_r)}{\partial\varepsilon_{mut}} = -jY_c\frac{1}{1+\cos\phi(\omega_{ro})}\frac{\partial\phi_{ref}}{\partial\varepsilon_{mut}}$$
$$\frac{\partial Y(\omega_r)}{\partial\omega} = -jY_c\frac{1}{1+\cos\phi(\omega_{ro})}\frac{\partial\phi_{ref}}{\partial\omega} \qquad (14)$$

So the derivative of ω_r with respect to ε_{mut} is:

$$\frac{\partial\omega_r}{\partial\varepsilon_{mut}} = -\frac{\partial\phi_{ref}}{\partial\varepsilon_{mut}}\left(\frac{\partial\phi_{ref}}{\partial\omega}\right)^{-1} \qquad (15)$$

We will initially consider the simplest case of a λ/2 resonator. In this case, $\phi_{ref} = -2\phi_1(\omega,\varepsilon_{mut})$ and:

$$\frac{\partial\phi_{ref}}{\partial\omega} = \frac{2\pi}{\omega_{ro}}, \quad \frac{\partial\phi_{ref}}{\partial\varepsilon_{mut}} = \frac{\pi}{\varepsilon_{eff}(1,W_1/h)}\frac{1-F_1}{2} \qquad (16)$$

Therefore, the sensitivity is:

$$\frac{\partial\omega_r}{\partial\varepsilon_{mut}} = -\frac{\omega_{ro}(1-F_1)}{4\varepsilon_{eff}(1,W_1/h)} = -\frac{\omega_{ro}}{2}\frac{1}{1+\dfrac{1+F_1}{1-F_1}\varepsilon_r} \qquad (17)$$

In agreement with our previous discussions, the sensitivity increases for lower F_1 and, thus, for a narrower width W_1. For $W_1 = 3.77$ mm, the frequency sensitivity is $\partial f_r / \partial\varepsilon_{mut} = -9.6\cdot10^7$ Hz where $f_r = \omega_r/(2\pi)$. This value agrees with the tangent at $\varepsilon_{mut} = 1$ of the numerical curve obtained through (10), shown in Fig. 4(a).

In the case of two sections, we can obtain ϕ_{ref} by introducing $Y_{in,2}$ in the expression for the reflection coefficient $\Gamma = (Y_c - Y_{in,2})/(Y_c + Y_{in,2})$ and calculating the corresponding phase. Then, the sensitivity of the resonance frequency ω_r to ε_{mut} is obtained from:

$$\frac{\partial\phi_{ref}(\phi_1,\phi_2)}{\partial\varepsilon_{mut}} = \frac{\partial\phi_{ref}(\phi_1,\phi_2)}{\partial\phi_1}\frac{\partial\phi_1}{\partial\varepsilon_{mut}} + \frac{\partial\phi_{ref}(\phi_1,\phi_2)}{\partial\phi_2}\frac{\partial\phi_2}{\partial\varepsilon_{mut}}$$
$$\frac{\partial\phi_{ref}(\phi_1,\phi_2)}{\partial\omega} = \frac{\partial\phi_{ref}(\phi_1,\phi_2)}{\partial\phi_1}\frac{\partial\phi_1}{\partial\omega} + \frac{\partial\phi_{ref}(\phi_1,\phi_2)}{\partial\phi_2}\frac{\partial\phi_2}{\partial\omega} \qquad (18)$$

The derivatives of ϕ_{ref} with respect to the electrical lengths are:

$$\frac{\partial\phi_{ref}(\phi_1,\phi_2)}{\partial\phi_1} = -2\frac{Y_{o2}^2}{Y_{1o}Y_c}, \quad \frac{\partial\phi_{ref}(\phi_1,\phi_2)}{\partial\phi_2} = -2\frac{Y_{o2}}{Y_c} \qquad (19)$$

On the other hand, the derivatives of ϕ_i in (18) with respect to ε_{mut} and ω are calculated from (4) in a straightforward manner. Replacing (19) and those derivatives in (18), one obtains:

$$\frac{\partial \omega_r}{\partial \varepsilon_{mut}} = -\frac{\omega_{ro}}{4}\frac{Y_{o2}\dfrac{1-F_1}{\varepsilon_{eff}(1,W_1/h)} + Y_{o1}\dfrac{1-F_2}{\varepsilon_{eff}(1,W_2/h)}}{Y_{o1}+Y_{o2}} =$$

$$= -\frac{\omega_{ro}}{2\left(Y_{o2}+Y_{o1}\right)}\left(\frac{Y_{o2}}{1+\dfrac{1+F_1}{1-F_1}\varepsilon_r} + \frac{Y_{o1}}{1+\dfrac{1+F_2}{1-F_2}\varepsilon_r}\right) \quad (20)$$

The two contributions in the bracket increase for a lower F_i, where i =1,2, and thus, for narrower W_i. Since W_1 is narrower than W_2, the factor F_1 is smaller than F_2 and because $Y_{o2} > Y_{o1}$, the first term will be dominant. Because we are adding two functions of the same sign, one can expect the sensitivity to be higher than the one obtained with the λ/2 resonator. For the widths $W_1 = 0.24$ mm, $W_2 = 3.77$ mm, the sensitivity is $\partial f_r / \partial \varepsilon_{mut} = -1.7 \cdot 10^8$ Hz, which agrees with the tangent at $\varepsilon_{mut} = 1$ of the numerical curve obtained through (10), shown in Fig. 4(a).

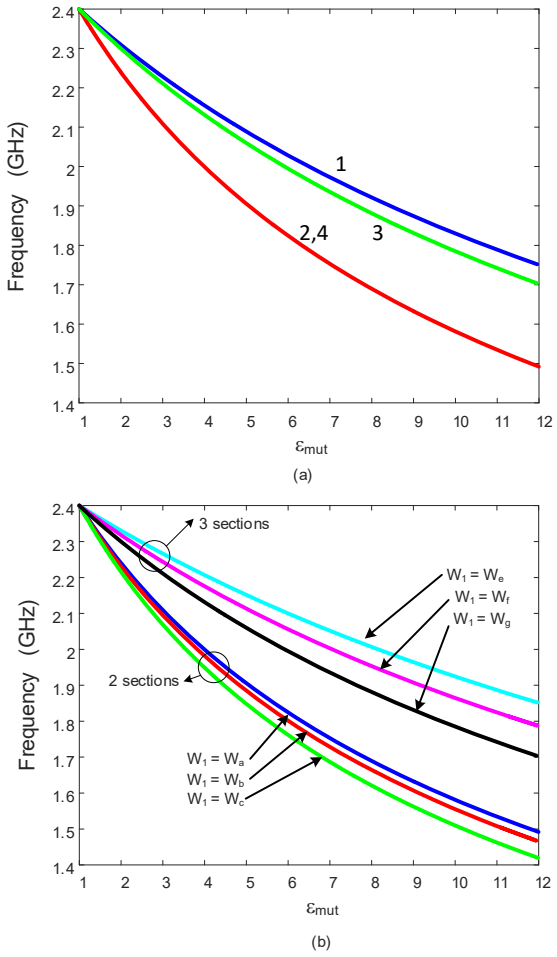

Fig. 4. Variation of the resonance frequency ω_r versus ε_{mut}. (a) Resonance frequency versus ε_{mut} for different numbers of sections in the step-impedance transmission line, calculated by obtaining the zero-value contour of (10). (b) Increase of the sensitivity of ω_r to ε_{mut} by reducing the width of some line sections. Details are given in the main text.

In the case of three sections, we will obtain ϕ_{ref} by introducing $Y_{in,3}$ in the expression for the reflection coefficient $\Gamma = (Y_c - Y_{in,3})/(Y_c + Y_{in,3})$. Following the same procedure, the sensitivity about $\varepsilon_{mut} = 1$ is given by:

$$\frac{\partial \omega_r}{\partial \varepsilon_{mut}} =$$

$$-\frac{\omega_{ro}}{4}\frac{{Y_{o2}}^2\dfrac{1-F_1}{\varepsilon_{eff}(1,W_1/h)} + Y_{o2}Y_{o1}\dfrac{1-F_2}{\varepsilon_{eff}(1,W_2/h)} + 2{Y_{o1}}^2\dfrac{1-F_1}{\varepsilon_{eff}(1,W_1/h)}}{{Y_{o2}}^2 + Y_{o2}Y_{o1} + 2{Y_{o1}}^2} =$$

$$-\frac{\omega_{ro}}{2({Y_{o2}}^2 + Y_{o2}Y_{o1} + 2{Y_{o1}}^2)}\left(\frac{{Y_{o2}}^2 + 2{Y_{o1}}^2}{1+\dfrac{1+F_1}{1-F_1}\varepsilon_r} + \frac{Y_{o2}Y_{o1}}{1+\dfrac{1+F_2}{1-F_2}\varepsilon_r}\right) \quad (21)$$

Let us compare the two terms in the bracket. Their denominators depend, respectively, on F_1 and F_2. However, the numerators depend on both Y_{o1} and Y_{o2}. In this case, W_1 is wider than W_2 (see Fig. 1), providing $Y_{o1} > Y_{o2}$ and $F_1 > F_2$. The influence of the admittance components in the numerator is stronger than those of F_i in the denominator, so the first term will be the dominant contribution. For the widths $W_1 = 3.77$ mm, $W_2 = 0.24$ mm, the sensitivity is $\partial f_r / \partial \varepsilon_{mut} = -10^8$ Hz, which agrees with the tangent at $\varepsilon_{mut} = 1$ of the numerical curve obtained through (10), shown in Fig. 4(a). This sensitivity is higher than the one obtained with a λ/2 resonator.

The analysis has been extended to the case of four sections and the resonance curve is overlapped with the one obtained with two sections [Fig. 4(a)]. One can also observe that the sensitivity of ω_r to ε_{mut}, is higher for an even number of sections than for one and three sections. Note that in the case of an odd number of sections the structure is not homogeneous since, for three sections, the most external (open-ended) section (Fig. 1) has the electrical length π instead of π/2 (in the absence of the MUT).

As gathered from (17)–(21) and (3), the sensitivity to ε_{mut} can be modified by reducing the width of some line sections. In the case of two sections, the sensitivity increases most by reducing the width W_1, affecting the first term of (20). As an example, in Fig. 4(b), we have considered the W_1 values: $W_a = 0.2339$ mm, $W_b = 0.1339$ mm, $W_c = 0.0339$ mm, whereas the width W_2 of the internal section has been kept constant at $W_2 = 3.7736$ mm. In the case of three sections, the resonance frequency is more sensitive to the width of the low impedance sections W_1, and the sensitivity increases by reducing this width. As an example, in Fig. 4(b), we have considered the following values of the first- and third-section width (W_1): $W_e = 7.77364$ mm, $W_f = 5.77364$ mm, $W_g = 3.77364$ mm, whereas the central-section width has been kept constant at $W_2 = 0.233915$ mm.

Note that for the oscillator design we will be interested in the admittance $Y_{in,n}(\varepsilon_{mut}, \omega_r)$. Although the functions $\omega_r(\varepsilon_{mut})$ are either quite similar (for one and three sections) or totally overlapped (for two and four sections), the frequency derivative $\partial \,\mathrm{Im}\left[Y_{in,n}(\varepsilon_{mut}, \omega_r)\right]/\partial\omega$ along each resonance curve versus ε_{mut} strongly depends on the number n of sections. This can be seen in Fig. 5 where contours of constant frequency derivative have been traced over the resonance curves. The derivative increases with the number n of sections. For three sections it is

more than one order of magnitude higher than the one obtained with one section. It is interesting to note that the resonance curves cross the constant-derivative contours near their turning points. Those contours are defined by the condition:

$$\frac{\partial Y_{in,n}(\omega(\varepsilon_{mut},c),\varepsilon_{mut})}{\partial\omega}=c \qquad (22)$$

where c is the value of the constant derivative. Because of the constant value on the right-hand side, the following condition is fulfilled:

$$\frac{\partial^2 Y_{in,n}(\omega(\varepsilon_{mut},c),\varepsilon_{mut})}{\partial\omega^2}d\omega+\frac{\partial^2 Y_{in,n}(\omega(\varepsilon_{mut},c),\varepsilon_{mut})}{\partial\omega\,\partial\varepsilon_{mut}}d\varepsilon_{mut}=0 \qquad (23)$$

And we can obtain the derivative $\partial\omega(\varepsilon_{mut},c)/\partial\varepsilon_{mut}$ as:

$$\frac{\partial\omega(\varepsilon_{mut},c)}{\partial\varepsilon_{mut}}=-\frac{\dfrac{\partial^2 Y_{in,n}(\omega(\varepsilon_{mut},c),\varepsilon_{mut})}{\partial\omega\,\partial\varepsilon_{mut}}}{\dfrac{\partial^2 Y_{in,n}(\omega(\varepsilon_{mut},c),\varepsilon_{mut})}{\partial\omega^2}} \qquad (24)$$

which will be infinite at the turning points. On the other hand, as observed in Fig. 2, for each ε_{mut} the point $\omega_r(\varepsilon_{mut})$, corresponding to the resonance frequency, approximately fulfils:

$$\frac{\partial^2 Y_{in,n}(\omega_r(\varepsilon_{mut}),\varepsilon_{mut})}{\partial\omega^2}\simeq 0 \qquad (25)$$

Thus, the resonance curve will cross the constant derivative contours very close to the turning points of these contours. In the case of three sections, the contours are narrower, with a smaller frequency variation, which gives rise to more noticeable differences between the crossing points and the turning points.

III. Oscillator Design

In this section the passive structure will be connected to the active network to obtain an oscillator circuit [Fig. 6(a)]. In the oscillator based on a slow-wave structure of [13], a lower phase noise was achieved when connecting this structure to the gate node, so this is the node where the sensing structure will be introduced here [Fig. 6(b)]. The active network contains the device, feedback elements and output load, as well as a bandpass-filtering stage at the analysis node. This is used to both ensure the validity of the semi-analytical formulation and prevent oscillations at higher resonance frequencies of the sensing structures. The active network will be the same in all cases, which will allow a thorough comparison of the oscillator performance with the various passive structures considered in Section II. This comparison will be carried out in terms of the sensitivity of the oscillation frequency and amplitude to ε_{mut}, and the phase-noise behavior.

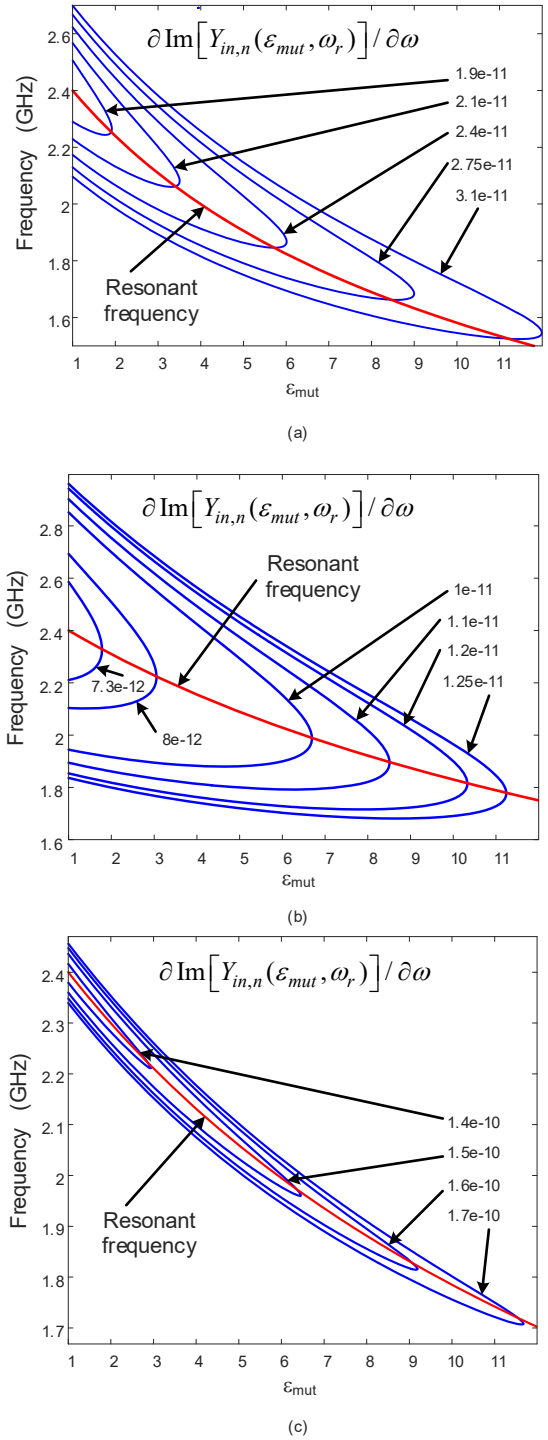

Fig. 5. Frequency selectivity. Constant frequency-derivative $\partial\,\mathrm{Im}\left[Y_{in,n}(\varepsilon_{mut},\omega_r)\right]/\partial\omega$ contours superimposed on the curves that provide the resonance frequency (ω_r) versus ε_{mut}. The frequency derivative increases with the number n of sections. (a) One section ($\lambda/2$ resonator). (b) Two sections. (c) Three sections.

The active network will be described with the nonlinear admittance function $Y_N(V,\omega)$, where V and ω are, respectively, the excitation amplitude and frequency. The function $Y_N(V,\omega)$ is extracted from HB by means of an auxiliary generator (AG) [36]-[40], introduced at the node where the sensing structure is connected (the gate terminal in

this case). A double sweep is performed in the AG frequency ω and amplitude V [Fig. 4(b)], obtaining the ratio between the AG current and amplitude [36]-[40]. Although this HB analysis must be carried out with a suitable number NH of harmonic terms, the function Y_N may be extracted at the fundamental frequency only, provided there are sufficient harmonic filtering effects at the AG location. This is discussed in the next sub-section.

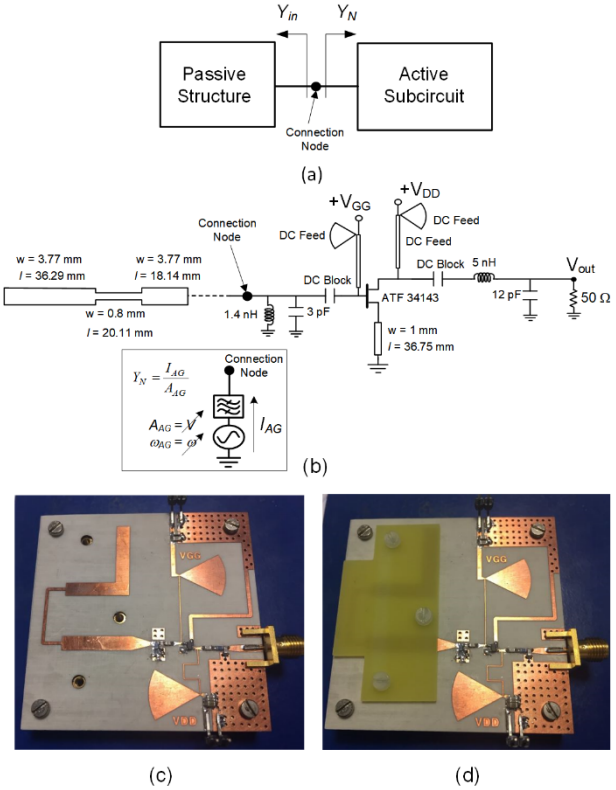

Fig. 6. Oscillator used for sensing applications. (a) Decomposition into an active sub-circuit and passive-linear one, corresponding to the sensing structure. (b) Schematic in the case of a three-section transmission line. (c) Photograph of the prototype built on Rogers 4003C ($\varepsilon_r = 3.55$, $h = 32$ mils). (d) Photograph of the prototype with an FR4 substrate placed over the sensing structure.

A. Steady-state solution

When combining $Y_N(V,\omega)$ with the linear admittance of the passive structure, one obtains the following steady-state oscillation condition:

$$Y_T = Y_N(V,\omega) + Y_{in,n}(\omega,\varepsilon_{mut}) = 0 \qquad (26)$$

As already indicated, $Y_N(V,\omega)$ is calculated in HB under multiple harmonic terms (NH = 7 in this case). Then, (26) considers the impact of the structure at the fundamental frequency, disregarding its effect at the second and higher harmonic terms. Provided the harmonic content is low at the node where the structure is connected in parallel (analysis node), the presence of the structure at the second and higher harmonic frequencies will have a small impact on the circuit solution. In fact, the nonlinear semi-analytical formulation will constitute a very good approach, as will be extensively verified through a rigorous comparison with HB under multiple harmonic terms.

Note that the frequency dependence of the active core Y_N is inherent to any oscillator, as this will contain reactive elements in its devices, as well as in its termination and matching networks. This frequency dependence will limit the negative conductance $Y_{N,r}(V=0,\omega) < 0$ to the desired operation band. Thus, it will prevent oscillator instabilities due to the onset of additional modes, which would result from resonances at frequencies different from the intended one. The complex equation (26) can be split into real and imaginary parts:

$$\begin{aligned} Y_{T,r} &= Y_{N,r}(V,\omega) = 0 \\ Y_{T,i} &= Y_{N,i}(V,\omega) + Y_{in,n,i}(\omega,\varepsilon_{mut}) = 0 \end{aligned} \qquad (27)$$

where the subscripts r and i indicate real and imaginary parts. Under the purely imaginary models in (1), the first equation does not depend on ε_{mut}. On the other hand, the imaginary part $Y_{N,i}(V,\omega)$ may give rise to a shift of the oscillation frequency with respect to the resonance frequency of the passive structure. This shift will be smaller for a higher frequency derivative of $Y_{in,n,i}(\omega,\varepsilon_{mut})$.

Because Y_N in (27) is a numerical function and both the real and imaginary parts are coupled through their dependences on V and ω, one cannot obtain an analytical expression of the oscillation frequency. However, the semi-analytical system (27) can be solved through a contour intersection procedure. The analysis is carried out by sweeping ε_{mut} and obtaining for each ε_{mut} the intersections between the zero value contours $Y_{T,r} = 0$ and $Y_{T,i} = 0$, which will provide the system solutions. For instance, Fig. 7 shows the intersection of the zero-value contours $Y_{T,r} = 0$ and $Y_{T,i} = 0$, obtained for one section ($\lambda/2$ resonator) and three sections, and $\varepsilon_{mut} = 1$. Those contours are traced in the plane defined by ω and V. The intersection point provides, in each case, the steady-state solution for $\varepsilon_{mut} = 1$. The contour $Y_{T,i} = 0$ [see (27)] is nearly independent of V because for all V the frequency derivative of $Y_{in,n,i}(\omega,\varepsilon_{mut})$ is much higher than that of $Y_{N,i}(V,\omega)$, which keeps the zero crossing nearly constant.

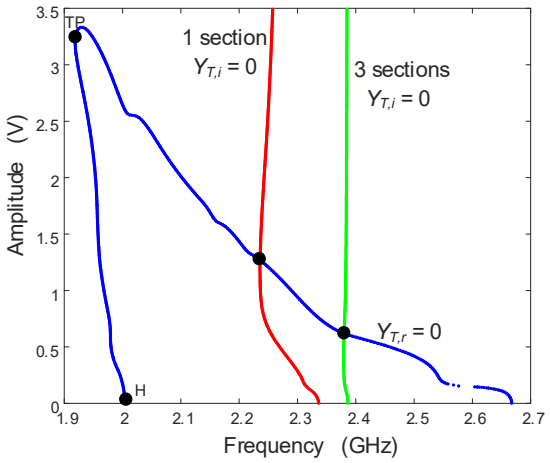

Fig. 7. Intersection of the zero value contours $Y_{Tr} = 0$ and $Y_{Ti} = 0$; the latter have been obtained for one section ($\lambda/2$ resonator) and three sections, and $\varepsilon_{mut} = 1$. The contour $Y_{T,i} = 0$ is nearly independent of V because for all V the frequency derivative of $Y_{in,n,i}(\omega,\varepsilon_{mut})$ is much higher than that of $Y_{N,i}(V,\omega)$. The Hopf bifurcation and turning point are also indicated.

The variation of the oscillation frequency and amplitude is obtained by representing the sequence of intersections points (of the kind shown in Fig. 7) versus ε_{mut}. Fig. 8 presents the results obtained for one, two and three sections. For $\varepsilon_{mut} = 1$, the resonance frequency of all the passive structures is 2.4 GHz. However, the oscillation frequency [Fig. 8(a)] will undergo a shift if the frequency derivative of $Y_{in,n,i}(\omega, \varepsilon_{mut} = 1)$ is not sufficiently high. This can be seen in Fig. 8(a) and (b) where the oscillation frequency at $\varepsilon_{mut} = 1$ agrees with 2.4 GHz for $n = 3$ and 4. For $n = 1$ and 2 [Fig. 8(b)] there is a downward shift at $\varepsilon_{mut} = 1$ due to the positive value of $Y_{N,i}(V, \omega)$ at 2.4 GHz. Attention should also be paid to the reduction of the ε_{mut} excursion with the number of stages, explained later in this section.

One can also compare the sensitivity of the oscillation frequency with respect to ε_{mut} with that of the resonance frequency, obtained in the previous section. Let a steady-state oscillation V_o, ω_o for $\varepsilon_{mut} = 1$ (corresponding to a particular structure) be assumed. Considering a small increment in ε_{mut}, so that the oscillation condition is still fulfilled, one can approach:

$$\begin{aligned} &\frac{\partial Y_{N,r}(V_o,\omega_o)}{\partial V}\Delta V + \frac{\partial Y_{N,r}(V_o,\omega_o)}{\partial \omega}\Delta\omega = 0 \\ &\frac{\partial Y_{N,i}(V_o,\omega_o)}{\partial V}\Delta V + \left(\frac{\partial Y_{N,i}(V_o,\omega_o)}{\partial \omega} + \frac{\partial Y_{in,n,i}(\omega_o)}{\partial \omega}\right)\Delta\omega \\ &+ \frac{\partial Y_{in,n,i}(\omega_o)}{\partial \varepsilon_{mut}}\Delta\varepsilon_{mut} = 0 \end{aligned} \quad (28)$$

To obtain the oscillation-frequency sensitivity about $\varepsilon_{mut} = 1$ we will solve $\Delta\omega$ in terms of $\Delta\varepsilon_{mut}$. This provides the following expression:

$$\frac{\partial\omega}{\partial\varepsilon_{mut}} = -\frac{\dfrac{\partial Y_{N,r}}{\partial V}\dfrac{\partial Y_{in,n,i}}{\partial\varepsilon_{mut}}}{\det_o + \dfrac{\partial Y_N{}^r(V_o,\omega_o)}{\partial V}\dfrac{\partial Y_{in,n,i}(\omega_o,\varepsilon_{mut})}{\partial\omega}} \quad (29)$$

where:

$$\det_o = \left.\frac{\partial Y_N{}^r}{\partial V}\frac{\partial Y_N{}^i}{\partial\omega} - \frac{\partial Y_N{}^i}{\partial V}\frac{\partial Y_N{}^r}{\partial\omega}\right|_{V_o,\omega_o} \quad (30)$$

If the derivative $\partial Y_{in,n,i}/\partial\omega$ is sufficiently large, one can approach:

$$\frac{\partial\omega}{\partial\varepsilon_{mut}} \cong -\frac{\partial Y_{in,n,i}}{\partial\varepsilon_{mut}}\left(\frac{\partial Y_{in,n,i}}{\partial\omega}\right)^{-1} \quad (31)$$

which agrees with the sensitivity of the resonance frequency to ε_{mut} calculated in (13). For comparison, the variation of the resonance frequency ω_r versus ε_{mut} obtained with the standalone passive structures under $n = 3$ and $n = 4$ has been superimposed in Fig. 8(a). In agreement with (29) and (31), the oscillation frequency closely approaches the original resonance frequency.

The shape of the amplitude curve versus ε_{mut} [Fig. 8(c)] is nearly identical to that of the contour $Y_{N,r} = 0$ (Fig. 7) for all the numbers n of line sections. This is because of the quasi-linear relationship between the oscillation frequency ω and ε_{mut}, observed in Fig. 8(a). The figure is reversed because the oscillation frequency ω decreases with ε_{mut}. On the other hand, the amplitude is higher for larger ε_{mut} due to the associated reduction of the oscillation frequency. Because we have neglected the line losses in (1), the maximum amplitude is the same regardless of the number n of line sections.

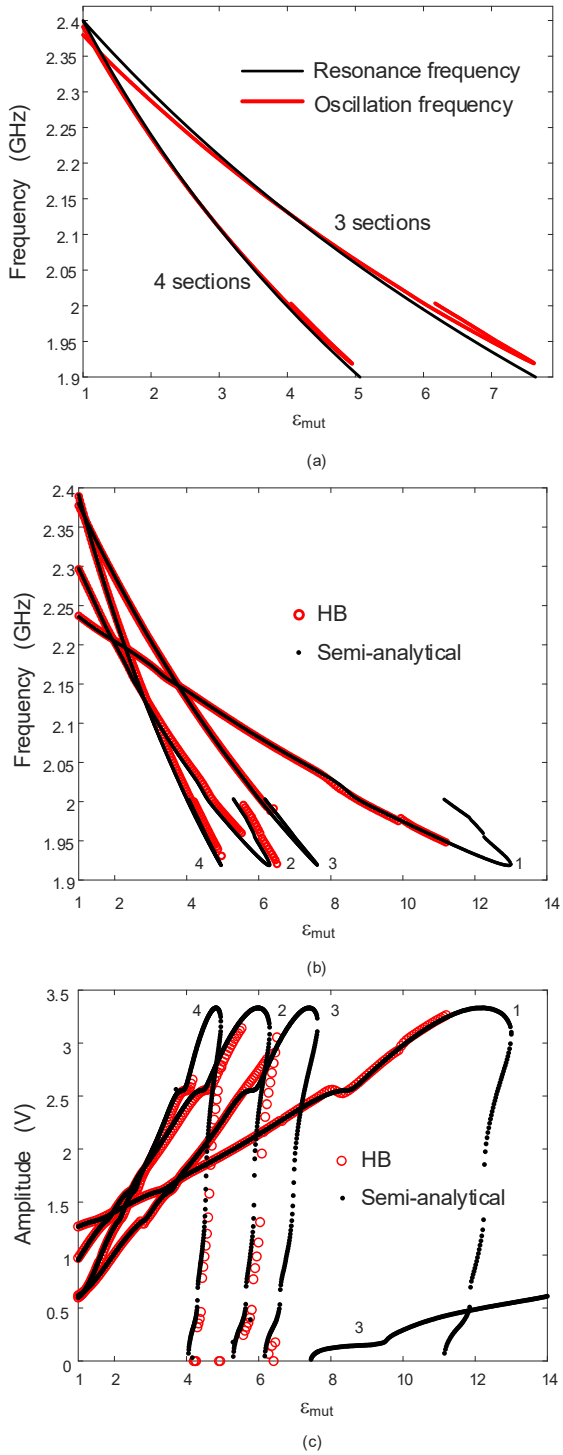

Fig. 8. Oscillator solution versus ε_{mut}, when considering ideal step-impedance resonators with different numbers n of sections and no losses. (a) Oscillation frequency and resonance frequency ω_r versus ε_{mut} for $n = 3, 4$. (b) Oscillation frequency. The solution calculated with (27) is validated with a default HB simulation (with NH = 7 harmonic terms), unable to complete the solution curves. (c) Oscillation amplitude, validated with HB.

Note that for $n = 3$ there is a second oscillation mode, associated with a higher resonance frequency, due to the longer delay. This resonance frequency is comprised within the frequency interval for which the oscillator active core exhibits a negative conductance; that interval is delimited by the two frequency values that fulfill $Y_{T,r}(V = 0,\ \omega) = 0$ in Fig. 7. The oscillation frequency (not represented) goes from 2.67 GHz to 2.38 GHz. This undesired higher-frequency mode arises from a stable DC solution through a supercritical Hopf bifurcation, so according to the bifurcation relationships [41]-[42], it must be stable at least near the bifurcation. The stability of the mode up to $\varepsilon_{mut} \cong 14$ has been verified using pole-zero identification [43]. However, as discussed in Section III, these stability properties change when considering a more realistic description of the three-section step-impedance transmission line.

The predictions by the semi-analytical equation (27) have been validated through their comparison with a default HB simulation, shown in Fig. 8(b) and Fig. 8(c). The number of harmonic terms considered (NH = 7) is the same used to extract the nonlinear function $Y_N(V,\omega)$. The HB simulation fails to provide the top regions of the solution curves, due to their proximity to the turning point (point of infinite slope). This is because of the ill conditioning of the Jacobian matrix of the HB system, which becomes singular at the turning point [44]-[47]. For the rest of the solution curve there is an excellent agreement between the results of the semi-analytical equations (27) and HB.

B. Hopf and turning-point bifurcations

The frequency dependence of $Y_{N,r}(V,\omega)$ in (27) will have a significant impact on the edges of the oscillation frequency interval. In fact, it provides the frequency of the Hopf bifurcation [41]-[45] at which the steady-state oscillation is extinguished, with a zero steady-state amplitude $V = 0$, when increasing ε_{mut}. Note that in the well-behaved oscillator, one will have negative conductance $Y_{N,r}(V = 0,\omega) < 0$ [46] in a single frequency band, so there will be only two frequency values, $\omega_{H,1}$ and $\omega_{H,2}$, providing the boundaries of this band.

Under the (purely imaginary) model (1), no matter the sensing structure used, the Hopf bifurcations will be obtained from the scalar equation:

$$Y_{N,r}(0,\omega_H) = 0 \tag{32}$$

Because the circuit should exhibit a steady-state oscillation with $V > 0$ for $\varepsilon_{mut} = 1$, we have only one Hopf bifurcation frequency ω_H for each sensing structure (in the targeted operation band). In fact, ω_H should be smaller than the oscillation frequency at $\varepsilon_{mut} = 1$. This is because the resonance frequency decreases with ε_{mut}. It is relevant to note that the frequency ω_H agrees with the lowest frequency (2 GHz) at which the contour $Y_{N,r}(V,\omega) = 0$ (shown in Fig. 7) exhibits $V = 0$. Note that the highest frequency providing $V = 0$ (2.67 GHz) cannot be reached for $\varepsilon_{mut} \geq 1$.

Even though ω_H is independent of the structure, the ε_{mut} value at which ω_H is reached does depend on the structure. This explains the oscillation extinction at different ε_{mut} values seen in Fig. 8. To directly obtain the ε_{mut} value at which the Hopf bifurcation takes place, we will replace ω_H in $Y_{T,i} = 0$ of (27) under $V = 0$ (condition for the oscillation extinction). This provides the scalar equation:

$$Y_{N,i}(0,\omega_H) + Y_{in,n,i}(\omega_H,\varepsilon_{mut}) = 0 \tag{33}$$

As an example, we will consider the case of the λ/2 resonator. Neglecting, for simplicity, the dependence of Y_{o1} on ε_{mut}, the Hopf bifurcation will be obtained at the following ε_{eff} value:

$$\varepsilon_{eff}(\varepsilon_{mut},W_1) = \left(\frac{\varepsilon_{eff}(W_1)\omega_{ro}}{\phi_{o1}\omega_H}\right)^2 \operatorname{arctg}^2\left(-Y_{N,i}(0,\omega_H)/Y_{o1}\right) \tag{34}$$

Similar expressions, though more complex, are obtained for $n > 1$. The Hopf bifurcations occur at the ε_{mut} values seen in Table I. Because under a sufficiently high derivative $\partial Y_{in,n,i}(\omega,\varepsilon_{mut})/\partial\omega$ the oscillation-frequency curve and the resonance curve are nearly overlapped, the ε_{mut} value at the Hopf bifurcation ($V = 0$) will be smaller for structures with a higher sensitivity of ω_r to ε_{mut}. This is because, due to this higher sensitivity, they will reach ω_H for a lower ε_{mut}, as shown in Fig. 8(a) and (b).

Table I
DIELECTRIC CONSTANT OF THE MUT AT THE HOPF BIFURCATION

Number of sections	ε_{mut}
1	11.2
2	5.3
3	6.2
4	4

In all the cases studied here, there are oscillatory solutions [see Fig. 8(c)] for ε_{mut} values beyond the Hopf bifurcation (where $V = 0$). This is because this Hopf bifurcation (occurring at ω_H) is reached after a turning point of the solution curve [40]-[42]. Note that in a manner like the Hopf bifurcation, the turning point occurs at the same amplitude V_{TP} and frequency ω_{TP} regardless of the number n of line sections. This is again because the function $Y_{N,r}(V,\omega)$ does not depend on ε_{mut} and, thus, its zero-value contour $Y_{N,r}(V,\omega) = 0$, shown in Fig. 7, remains constant under the ε_{mut} variation. To demonstrate this, note that the contour $Y_{N,r}(V,\omega) = 0$ produces a curve $V = c_R(\omega)$ (Fig. 7) that exhibits an infinite-slope point $TP = (\omega_{TP},V_{TP})$, fulfilling $dc_R(\omega_{TP})/d\omega = \infty$. On the other hand, the equation $Y_{T,i}(V,\omega,\varepsilon_{mut}) = 0$ produces a curve $V = c_I(\omega,\varepsilon_{mut})$ that shifts leftwards when increasing ε_{mut}, which leads to a reduction of the oscillation frequency [Fig. 8(a)]. At $\varepsilon_{mut} = \varepsilon_{mut}^{TP}$, the curve $V = c_I(\omega,\varepsilon_{mut})$ becomes tangent to the point TP and fulfils $dc_I(\omega_{TP},\varepsilon_{mut}^{TP})/d\omega = \infty$. Through a perturbation analysis of $Y_{T,r}$ and $Y_{T,i}$, it is straightforward to demonstrate that:

$$\frac{\partial Y_{N,r}(V_{TP},\omega_{TP})}{\partial V}=0,\quad \frac{\partial Y_{T,i}(V_{TP},\omega_{TP},\varepsilon_{mut}^{TP})}{\partial V}=0 \qquad (35)$$

On the other hand, the formal condition for turning point will be the singularity of the Jacobian matrix of the steady-state system (27) with respect to V and ω. Due to the zero value of the derivatives (35) the determinant of this matrix is zero at the same oscillation frequency and amplitude (ω_{TP},V_{TP}) regardless of the sensing structure. Again, although the values (ω_{TP},V_{TP}) are independent of n, they will be reached for a different ε_{mut} with each structure. Under a higher sensitivity, the *TP* will be obtained for a smaller ε_{mut}, due to the faster shift to lower frequencies of $Y_{T,i}$.

In summary, for a higher n there will be a reduction of the measurable ε_{mut} range. However, there will also be a higher sensitivity and, as shown in the next subsection, a lower phase-noise spectral density.

C. Phase-noise spectral density

As stated in the introduction, a low phase-noise spectral density will be fundamental for an accurate and reliable material characterization. Departing from the steady-state system (27), one can perform an approximate calculation of the phase-noise spectrum by introducing into this system a small-amplitude perturbation; this will give rise to the increments $V_o+\delta V$, ω_o+s, where V_o and ω_o are the steady-state amplitude and frequency and s acts like a time differentiator [46]. The perturbed system is:

$$\frac{\partial Y_N(V_o,\omega_o)}{\partial V}\delta V+\frac{\partial\left[Y_N(V_o,\omega_o)+Y_{in,n}(\omega,\varepsilon_{mut})\right]}{\partial\omega}\left(-j\frac{\delta\dot{V}}{V_o}+\delta\dot{\phi}\right)=I_N(t) \qquad (36)$$

where $I_N(t)$ is an equivalent noise current source, connected at the node where the planar structure is introduced. Splitting (36) into real and imaginary parts and applying the Fourier transform, one derives the following expression for the phase-noise spectral density:

$$\left\langle\left|\Delta\phi(\Omega)\right|^2\right\rangle=\frac{\left|\frac{\partial Y_N(V_o,\omega_o)}{\partial V}\right|^2\frac{2\left\langle\left|I_N\right|^2\right\rangle}{{V_o}^2}}{\Omega^2\left(\det{}_o+\frac{\partial {Y_N}^r(V_o,\omega_o)}{\partial V}\frac{\partial Y_{in,n,i}(\omega_o,\varepsilon_{mut})}{\partial\omega}\right)^2} \qquad (37)$$

where $\left\langle\left|I_N\right|^2\right\rangle$ is the spectral density of the equivalent current noise source (calculated at the analysis node following the procedure in [47]) and Ω is the offset frequency from the oscillator carrier. We should also note that in a well-behaved oscillator we will have $\partial {Y_N}^r/\partial V>0$ [38]-[39]. On the other hand, from the inspection of (37), the phase noise will decrease with the derivative $\partial Y_{in,n,i}/\partial\omega$. As shown in Fig. 5, this derivative increases with the number of stages and with ε_{mut}. However, we must keep in mind that the variation of ε_{mut} affects both the oscillation amplitude and frequency (Fig. 8) and, as a result, will give rise to changes in $\partial Y_N/\partial V$ and $\partial Y_N/\partial\omega$.

In (37), the derivatives of the functions $Y_N(V,\omega)$ and $Y_{in,n,i}(\omega)$ with respect to V and ω are calculated numerically. In fact, each of these functions constitutes a mesh that should be dense enough to allow a derivative calculation through finite differences using the values adjacent to each point (V, ω). Fig. 9 presents the variation of the phase-noise spectral density at the constant offset frequency of 100 kHz versus ε_{mut} for different n values. As expected, the phase noise decreases with n and exhibits a fast growth near the turning point [40], occurring at a different ε_{mut} for each n. This is because the term in brackets in (37), agreeing with the determinant of the Jacobian matrix of (26), becomes zero at the turning point. In all cases, there are slight local maxima due the changes in the derivatives $\partial Y_N/\partial V$ and $\partial Y_T/\partial\omega$. The results obtained with (37) are compared with those based on HB simulations, using the conversion-matrix approach [48]-[49], at points with good convergence properties. As can be seen, there is a significant average noise reduction with the number of sections.

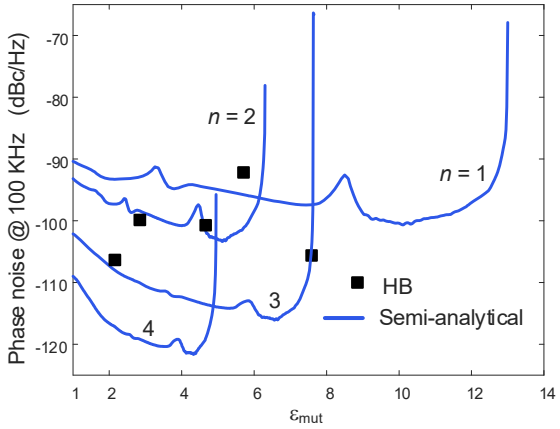

Fig. 9 Variation of the phase-noise spectral density at the constant offset frequency of 100 kHz versus ε_{mut} for different numbers n of sections of the sensing structure. The results obtained with (37) are compared with those based on HB simulations, using the conversion-matrix approach [41]-[42], at points with good convergence properties.

III. Practical Design

In this section a purely numerical analysis of the sensor oscillator will be carried out, based on realistic models of the transistor and the sensing structure. Both a three-section step-impedance transmission line and a slow-wave structure will be considered. Their input admittance will be described, in a general manner, with the numerical passive-linear admittance $Y_{in}(\omega,\varepsilon_{mut})$, which will have a real part different from zero: $Y_{in,r}(\omega,\varepsilon_{mut})\neq 0$ due to the presence of losses. The steady-state oscillation equations will be:

$$\begin{aligned}Y_{T,r}&=Y_{N,r}(V,\omega)+Y_{in,r}(\omega,\varepsilon_{mut})=0\\ Y_{T,i}&=Y_{N,i}(V,\omega)+Y_{in,i}(\omega,\varepsilon_{mut})=0\end{aligned} \qquad (38)$$

Unlike the situation in Section II, in the presence of losses, the maximum oscillation frequency ω_H will depend on the structure and its number n of sections. The admittance $Y_{in}(\omega,\varepsilon_{mut})$ will be calculated by making use of a multilayer

model and through electromagnetic (EM) simulations. The multilayer model is based on the method of moments and the Green's function method [25].

A. Three-section step-impedance transmission line

In the presence of a realistic model of the three-section step-impedance transmission line (including losses), the zero-value contour of the total admittance $Y_{T,r}=0$ will depend on ε_{mut}, as seen in Fig. 10, where the collection of zero-value contours $Y_{T,r}(V,\omega,\varepsilon_{mut})=0$ obtained for ε_{mut} going from 1 to 10 has been represented. For the host transmission line in Rogers 4003C we have taken the actual value of the loss tangent, $\tan\delta=0.0024$, and for the MUT we have assumed a constant value: $\tan\delta_{mut}=0.002$, in a manner like what is done in [1]. The contour obtained in the absence of losses, with a higher amplitude, is also shown for comparison. For all the ε_{mut} values, the contours in the presence of losses lie inside the lossless contour. These contours exhibit a continuous evolution and are composed by two distinct curves for most ε_{mut} values. Note that the losses will also reduce the sensitivity of the resonance frequency ω_r to ε_{mut}, as will be shown next. Nevertheless, the main qualitative characteristics of the oscillator behavior will be the same.

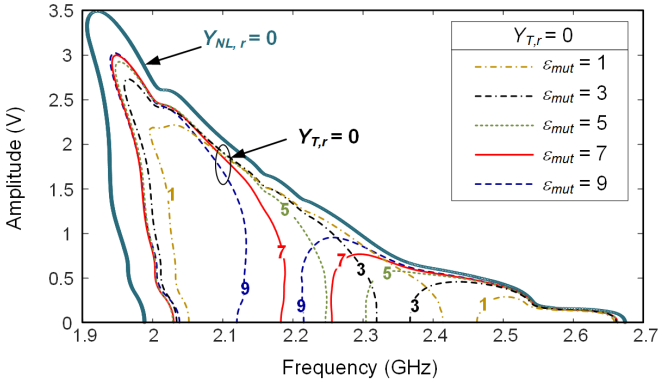

Fig. 10. Collection of zero-value contours of the real part of the total admittance $Y_{T,r}(V,\omega,\varepsilon_{mut})=0$ under a realistic description of a three-section step-impedance transmission line, obtained for ε_{mut} going from 1 to 10. It can be compared with the one obtained in the absence of losses, with a similar qualitative shape.

Solving (38) through contour intersections one obtains the variation of the oscillation amplitude and frequency versus ε_{mut} shown in Fig. 11. The low-amplitude higher frequency mode detected in Fig. 8 for $n=3$ is still present in this practical implementation. However, now this undesired mode arises from an unstable DC solution through a supercritical Hopf bifurcation. Thus, according to the bifurcation relationships [41]-[42], it must be unstable (physically unobservable) at least near the bifurcation. Using pole-zero identification [43], we have verified that it is unstable up to $\varepsilon_{mut}\cong 11$. In the experiment this mode did not cause any problems. The frequency sensitivity about $\varepsilon_{mut}=1$ is $\partial f/\partial\varepsilon_{mut}=-5.87\cdot10^{7}$ Hz. The resonance frequency ω_r of the standalone three-section line in the presence of losses is nearly overlapped, so the oscillator properly follows this resonance frequency. In the absence of losses, the frequency sensitivity was $\partial f/\partial\varepsilon_{mut}=-10^{8}$ Hz, so there has been a sensitivity reduction to nearly one half of the original value. This reduction allows increasing the range of measurable ε_{mut} values. Without losses, the Hopf bifurcation was obtained at $\varepsilon_{mut}=6.2$; with losses it is obtained at $\varepsilon_{mut}=9.94$. As in the analyses of Section III, we have compared the results of (38) with those obtained with default HB; they are fully overlapped in regions where HB achieves convergence.

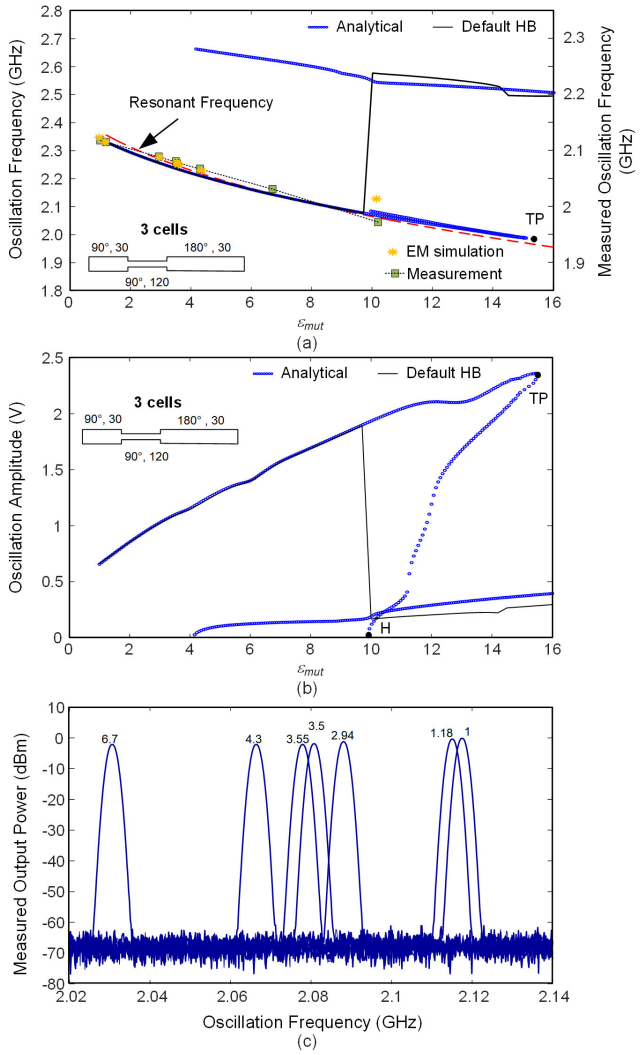

Fig. 11. Oscillator analysis in the presence of a three-section step-impedance transmission line, considering the line loss. The analysis is carried out by making use of a multilayer model and an EM simulation (discrete points). (a) Oscillation frequency versus ε_{mut} obtained through (38) and compared with the HB results. Measurement points are superimposed. (b) Oscillation amplitude, compared with the HB results. (c) Collection of experimental output spectra for the characterized ε_{mut} values.

EM simulations and measurements obtained when sensing the available substrates (with height larger than 3 mm following the recommendations in [5]-[8]) have been superimposed in the frequency curve. Note that there is a shift in the measured oscillation frequency with respect to the analysis prediction, which is attributed to inaccuracies in the package model of the active device. However, the variation pattern of the oscillation frequency versus ε_{mut} and the sensitivity exhibit an excellent

agreement. Fig. 11(c) shows the collection of experimental output spectra for the characterized ε_{mut} values. The output power variation in the range 1 to 6.7 is about 2.6 dB.

The collection of measured phase-noise spectra, obtained with the R&S FSWP8 Phase Noise Analyzer, when varying ε_{mut}, is shown in Fig. 12. A very limited variation of the phase-noise spectral density is obtained when changing ε_{mut}, and the phase-noise spectral densities are comprised between −110 dBc/Hz and −106.2 dBc/Hz at 100 kHz offset frequency and comprised between −135.5 dBc/Hz and −131 dBc/Hz at 1 MHz.

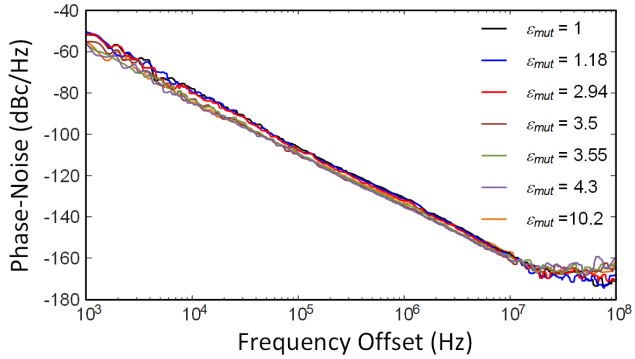

Fig. 12. Phase noise of the oscillator containing a three-section step-impedance transmission line. Collection of experimental phase-noise spectra when varying ε_{mut}. The spectra were measured with the R&S FSWP8 Phase Noise Analyzer.

As in [5]-[8], the sensor is intended for low-loss dielectric materials, so it is not optimized for the measurement of the complex permittivity of samples. However, a preliminary study of the impact of the imaginary part of the dielectric constant, denoted as ε_r'', has been carried out. We have calculated the oscillation frequency and amplitude versus ε_{mut} for different values of the imaginary part of the dielectric constant (Fig. 13). The two functions, $\omega(\varepsilon_{mut}, \varepsilon_r'')$ and $V(\varepsilon_{mut}, \varepsilon_r'')$ are univocal in this case (note that the lower curve sections are unstable), so provided a calibration is performed, one should be able to determine both ε_{mut} and ε_r'' from the measurement of the oscillation amplitude and frequency. The calibration requires using measurands with known values of the Debye-model parameters. Using these measurands, a nonlinear model, such as a neural network, can be developed from the input pairs (V, ω) and the output pairs (ε_{mut}, ε_r''). The resulting model should be able to predict ε_{mut} and ε_r'' of the material at the corresponding frequency ω. Due to the high frequency selectivity of $Y_{in,n,i}$, the oscillation frequency ω will nearly follow the same curve versus ε_{mut} obtained in the lossless analysis of Fig. 11(a). However, the increase of $Y_{in,r}(\omega, \varepsilon_{mut}, \varepsilon_r'')$ with ε_r'' reduces the oscillation ε_{mut} interval, since the inverse Hopf bifurcation is obtained for a smaller ε_{mut}. In principle, sufficient accuracy should be achieved by determining ε_{mut} from the value of the oscillation frequency and then ε_r'' from the oscillation amplitude, which depends on both ε_{mut} and ε_r''.

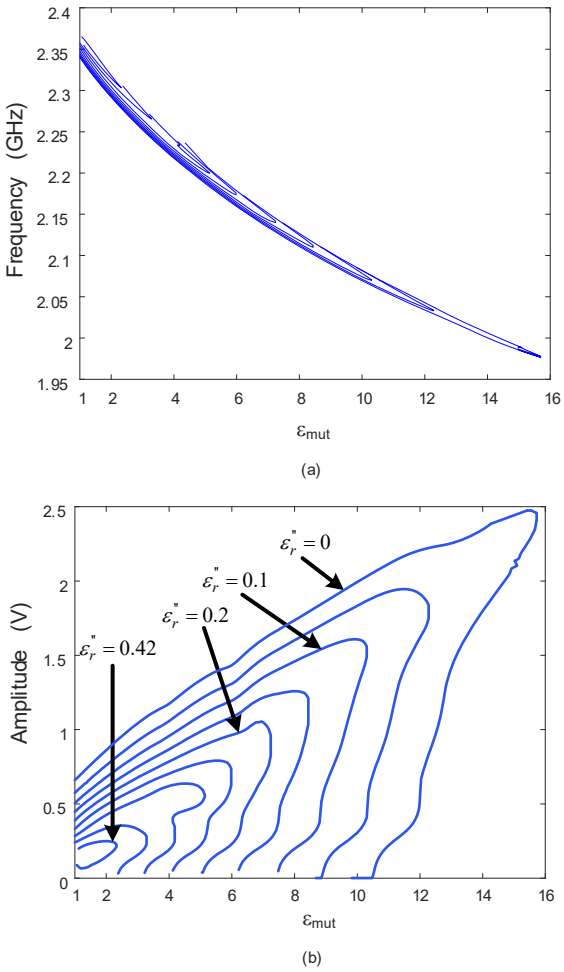

Fig. 13. Oscillator solution in the presence of losses in the MUT. (a) Oscillation frequency versus ε_{mut} for ε_r'' between 0 and 0.42. (b) Oscillation amplitude versus ε_{mut} for the same ε_r'' values.

B. Slow-wave structure

The slow-wave structures exhibit a high group delay, enabling a high-quality factor in a compact size [16]-[18]. This is obtained by increasing the effective capacitance and/or inductance of the line, which can be achieved through different strategies [16]-[18]. Here we will consider a slow-wave structure based on a unit cell consisting of a Schiffman-section [18], [13], providing an inductive effect, and an open-circuited stub, providing a capacitive effect. Due to the complexity of the structure, including a coupled-line section, an analytical study in terms of the number of cells in the vein of the one carried out for the step-impedance transmission line would be virtually impossible; nevertheless, a higher number of cells should increase the group delay and, as a result, the frequency sensitivity. However, it will also lead to higher losses and a larger size, so a compromise is necessary.

In this application, the parameters of the unit cell have been fitted to obtain a resonance frequency of 2.3 GHz with the group delay τ = 10.6 ns at ε_{mut} = 1 using six cells. This number of cells enables a compact size of 18.4 mm x 5.25 mm. Introducing the slow-wave structure in (38) and solving the oscillator equation through contour intersections, one obtains the oscillation frequency and amplitude shown in Fig. 14. As in

the case of step-impedance transmission line with $n = 3$, there is an unstable higher frequency mode, which arises at $\varepsilon_{mut} = 7.5$ and becomes stable at $\varepsilon_{mut} \cong 12$. In the experiment this mode did not cause any problems. The results of the semi-analytical formulation are overlapped with those obtained with default HB when it achieves convergence. This default HB jumps to the lower-amplitude mode in a discontinuous manner. In fact, the qualitative behavior is the same obtained with the three-section step-impedance transmission line; however, there is a higher frequency sensitivity, given by $\partial f / \partial \varepsilon_{mut} = -7.8 \cdot 10^7$ Hz, and the size is smaller. Note the slow-wave structure has not been optimized for this particular purpose; furthermore, other slow-wave configurations could provide better results, though such a study is beyond the scope of this work. Measurements obtained when sensing the available substrates have been superimposed in the frequency curve. As in the case of the three-section line, there is a shift in the oscillation frequency due to inaccuracies in the active-device model. However, the variation pattern of the oscillation frequency versus ε_{mut} and the sensitivity exhibit an excellent agreement. Fig. 14(c) shows the collection of experimental output spectra for the characterized ε_{mut} values. The output power variations in the range 1 to 6.7 is about 3.4 dB.

The phase-noise spectra obtained for the different ε_{mut} values are shown in Fig. 15(a). Note that for this slow-wave structure the dielectric constant $\varepsilon_{mut} = 10.2$ is very close to the oscillation boundary, in consistency with its higher frequency sensitivity. Except for $\varepsilon_{mut} = 10.2$, the phase-noise values are about 1 dB lower than in the case of the step-impedance transmission line. These results are well predicted by the analysis of Fig. 15(b), carried out through the semi-analytical formulation of Section II.C. As already stated, in that formulation, the double-entry admittance functions $Y_{T,r}(V,\omega)$ and $Y_{T,i}(V,\omega)$ are numerically differentiated with respect to V and ω. Measurements obtained when sensing the available substrates are superimposed with good agreement. As can be seen, the variations versus ε_{mut} are relatively small, as confirmed by the experimental results (superimposed). Note that, as in previous cases, there are slight local minima/maxima due the changes in the complex derivatives $\partial Y_N / \partial V$ and $\partial Y_T / \partial \omega$. In summary, the slow-wave structure enables a higher frequency sensitivity, with a lower phase-noise spectral density and smaller size.

To verify the impact of temperature we have performed temperature changes between 25º C and 50º C, without observing any significant differences in the measured spectrum. We have not been able to perform humidity variations in a controlled manner, but the system has been operating for three days without any relevant changes in the spectrum. On the other hand, the system has also been off for several days and when turning it on again a nearly identical spectrum has been obtained, so it is very repeatable.

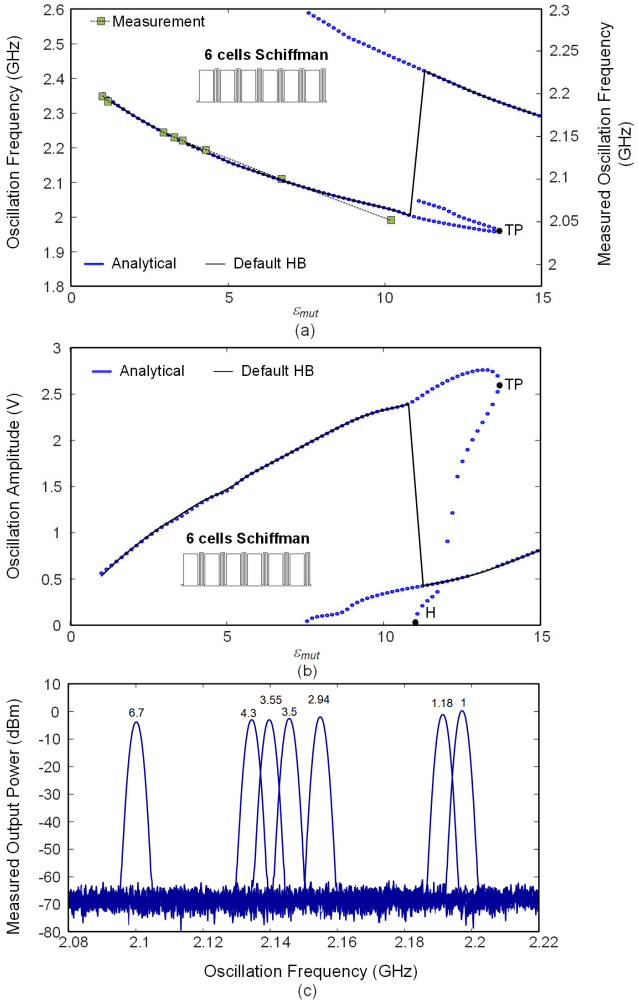

Fig. 14. Oscillator analysis in the presence of a slow-wave structure based on a Schiffman section (inset). The analysis is carried out by making use of a multilayer model and an EM simulation (discrete points). (a) Oscillation frequency versus ε_{mut} with HB results and measurements points superimposed. (b) Oscillation amplitude. (c) Collection of experimental output spectra for the characterized ε_{mut} values.

IV. Conclusions

An in-depth study of the capabilities of oscillators based on step-impedance transmission lines and slow-wave structures for the implementation of dielectric sensors has been carried out. The dielectric to be sensed is placed over the entire passive structure, which gives rise to a change in its resonance frequency. Initially, the sensitivity of this resonance frequency to the dielectric constant of the material under test (MUT) has been theoretically derived, under a lossless simplified model. Emphasis has been placed on the analysis of the effect of the number of line sections and on the frequency selectivity. The structures have been sequentially connected to the active core of an oscillator circuit, which has been kept unmodified for a fair comparison of the oscillator performance in the presence of the various structures. The active core is modeled with a nonlinear admittance function extracted from harmonic-balance simulations, which is added to the passive linear admittance of each sensing structure. In the absence of losses, all the oscillation curves are extinguished at the same frequency. However, this frequency will be obtained for a lower

dielectric constant of the MUT under a higher frequency sensitivity. In the case of structures with a high frequency sensitivity, the oscillation frequency is nearly superimposed to the resonance frequency, so the oscillator system should enable an easy detection of these frequency variations. In the presence of losses, there will be some quantitative changes in the performance, but the main qualitative properties remain unchanged: the oscillation-frequency sensitivity increases, and the phase-noise decreases with the frequency selectivity of the sensing structure. Very good results have been obtained in two different experimental implementations, using a three-section step-impedance transmission line and a slow-wave structure based on Schiffman section.

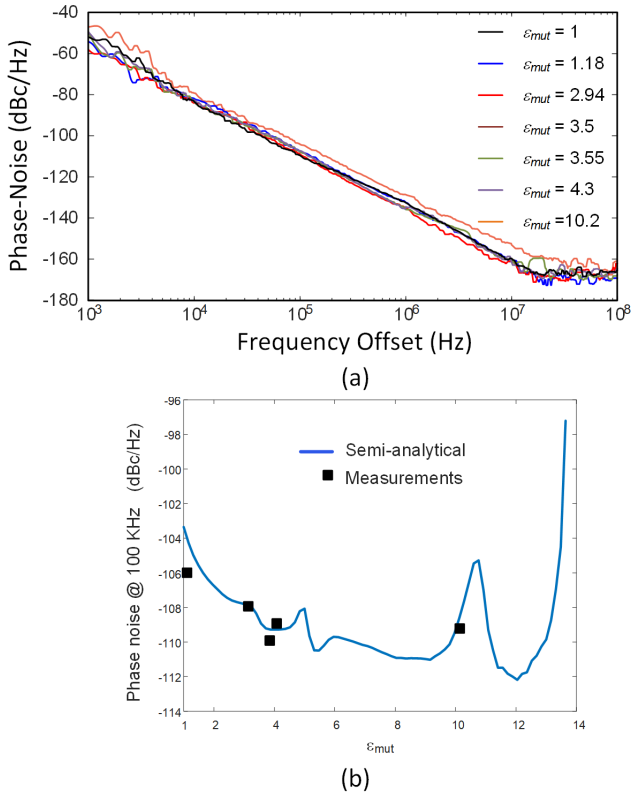

Fig. 15. Phase noise of the oscillator containing a slow-wave structure based on a Schiffman section. (a) Collection of experimental phase-noise spectra, when varying ε_{mut}. The spectra were measured with the R&S FSWP8 Phase Noise Analyzer. (b) Analysis of the phase-noise spectral density at the constant offset frequency 100 kHz, carried out with the semi-analytical formulation in Section II.C. Measurement points are superimposed.

ACKNOWLEDGMENT

The authors would like to thank Eva Cuerno and Paul Garcia for their valuable help in the manufacture of the different prototypes.

REFERENCES

[1] A. Ebrahimi, J. Scott and K. Ghorbani, "Differential Sensors Using Microstrip Lines Loaded With Two Split-Ring Resonators," *IEEE Sensors Journal*, vol. 18, no. 14, pp. 5786-5793, 15 July15, 2018.

[2] A. Ebrahimi, J. Scott and K. Ghorbani, "Transmission Lines Terminated With LC Resonators for Differential Permittivity Sensing," *IEEE Microwave and Wireless Components Letters*, vol. 28, no. 12, pp. 1149-1151, Dec. 2018.

[3] L. Su, J. Mata-Contreras, P. Vélez and F. Martín, "Splitter/Combiner Microstrip Sections Loaded With Pairs of Complementary Split Ring Resonators (CSRRs): Modeling and Optimization for Differential Sensing Applications," *IEEE Transactions on Microwave Theory and Techniques*, vol. 64, no. 12, pp. 4362-4370, Dec. 2016.

[4] J. Naqui, C. Damm, A. Wiens, R. Jakoby, L. Su, J. Mata-Contreras, F. Martín, "Transmission Lines Loaded With Pairs of Stepped Impedance Resonators: Modeling and Application to Differential Permittivity Measurements," *IEEE Transactions on Microwave Theory and Techniques*, vol. 64, no. 11, pp. 3864-3877, Nov. 2016.

[5] J. Muñoz-Enano, P. Casacuberta, L. Su, P. Vélez, M. Gil, F. Martín, "Open-Ended-Line Reflective-Mode Phase-Variation Sensors for Dielectric Constant Measurements," *Proc. IEEE Sensors* 2020, Rotterdam, The Netherlands, 25–28 October 2020.

[6] J. Muñoz-Enano, J. Coromina, P. Vélez, L. Su, M. Gil, P. Casacuberta, F. Martín, "Planar Phase-Variation Microwave Sensors for Material Characterization: A Review and Comparison of Various Approaches," *Sensors* 2021, 21, 1542.

[7] J. Muñoz-Enano, P. Vélez, L. Su, M. Gil, P. Casacuberta and F. Martín, "On the Sensitivity of Reflective-Mode Phase-Variation Sensors Based on Open-Ended Stepped-Impedance Transmission Lines: Theoretical Analysis and Experimental Validation," *IEEE Trans. Microw. Theory Techn.*, vol. 69, no. 1, pp. 308-324, Jan. 2021.

[8] J. Coromina; J. Muñoz-Enano; P. Vélez; A. Ebrahimi, J. Scott, K. Ghorbani, F. Martín, "Capacitively-Loaded Slow-Wave Transmission Lines for Sensitivity Improvement in Phase-Variation Permittivity Sensors," *50th European Microwave Conference (EuMC)*, 2021, pp. 491-494.

[9] A. Ebrahimi et al., "Highly Sensitive Phase-Variation Dielectric Constant Sensor Based on a Capacitively-Loaded Slow-Wave Transmission Line," *IEEE Trans Circuits Syst. I: Regul. Pap.*, vol. 68, no. 7, pp. 2787-2799, July 2021.

[10] V. Lammert et al., "A K-Band Complex Permittivity Sensor for Biomedical Applications in 130-nm SiGe BiCMOS," *IEEE Trans Circuits Syst. II: Express Br.,* vol. 66, no. 10, pp. 1628-1632, Oct. 2019.

[11] M. Hofmann, G. Fischer, R. Weigel and D. Kissinger, "Microwave-Based Noninvasive Concentration Measurements for Biomedical Applications," *IEEE Trans. Microw. Theory Techn*, vol. 61, no. 5, pp. 2195-2204, May 2013.

[12] B. Laemmle, K. Schmalz, J. C. Scheytt, R. Weigel and D. Kissinger, "A 125-GHz Permittivity Sensor With Read-Out Circuit in a 250-nm SiGe BiCMOS Technology," *IEEE Trans. Microw. Theory Techn*, vol. 61, no. 5, pp. 2185-2194, May 2013.

[13] M. Pontón, S. Sancho, A. Herrera, A. Suárez, "Nonlinear analysis of oscillators based on a slow-wave structure for phase-noise reduction," *IEEE MTT-S Int. Microw. Symp. Dig.*, Denver, CO, USA, 19-24 June 2022.

[14] A. K. Poddar, U. L. Rohde, "Slow Wave Resonator based tunable oscillators," *IEEE Int. Frequency Control and Europ. Frequency and Time Forum* (*FCS*) *Proc.*, San Francisco, CA, USA, 2011, pp. 1-10.

[15] S. Bourdel et al. "77.8 GHz Standing-wave Oscillator Based on a Tuneable Slow-wave Coplanar Stripline Resonator," *IEEE Int. New Circuits Syst. Conf.* (NEWCAS), 2020, pp. 18-21.

[16] M. Orellana, J. Selga, M. Sans, A. Rodríguez, V. Boria, F. Martín, "Synthesis of slow-wave structures based on capacitive-loaded lines through aggressive space mapping (ASM)," *Int. J. RF Microw. Comput. Aided Eng.* 2015, 25, 629–638.

[17] C. Zhou, H. Y. D. Yang, "Design Considerations of Miniaturized Least Dispersive Periodic Slow-Wave Structures," *IEEE Trans. Microw. Theory Techn.*, vol. 56, no. 2, pp. 467-474, Feb. 2008.

[18] W.S. Chang, C.Y. Chang, "A high slow-wave factor microstrip structure with simple design formulas and its application to microwave circuit design," *IEEE Trans. Microw. Theory Techn.*, vol. 60, no. 11, pp. 3376 –3383, Nov. 2012.

[19] K. Entesari, A. A. Helmy and M. Moslehi-Bajestan, "Integrated Systems for Biomedical Applications: Silicon-Based RF\Microwave Dielectric Spectroscopy and Sensing," *IEEE Microw. Mag.*, vol. 18, no. 5, pp. 57-72, July-Aug. 2017.

[20] M. Adhikary, A. Biswas and M. J. Akhtar, "Active Integrated Antenna Based Permittivity Sensing Tag," *IEEE Sens. Lett.*, vol. 1, no. 6, pp. 1-4, Dec. 2017.

[21] F. I. Jamal, S. Guha, M. H. Eissa, D. Kissinger and J. Wessel, "A low-power 30 GHz complex dielectric chem-bio-sensor in a SiGe BiCMOS technology," 2017 *First IEEE MTT-S Int. Microw. Bio Conf.* (*IMBIOC*), Gothenburg, Sweden, 2017, pp. 1-4.

[22] J. Wessel, K. Schmalz, J. C. Scheytt, B. Cahill and G. Gastrock, "Microwave biosensor for characterization of compartments in teflon capillaries," 2012 42nd *Europ. Microw. Conf.* (*EuMC*), 2012, Amsterdan, Netherlands, pp.534-537.
[23] J. Chien and A. M. Niknejad, "Oscillator-Based Reactance Sensors With Injection Locking for High-Throughput Flow Cytometry Using Microwave Dielectric Spectroscopy," *IEEE J. Solid-State Circuits*, vol. 51, no. 2, pp. 457-472, Feb. 2016.
[24] M. Pontón, S. Hernández and A. Suárez, "Phase-sensitivity analysis of injection-locked mutually coupled oscillators," 2017 47th *Europ. Microw. Conf.* (*EuMC*), 2017, Nuremberg, Germany, pp. 771-774.
[25] B. Kim *et al*., "A Proximity Coupling RF Sensor for Wrist Pulse Detection Based on Injection-Locked PLL," *IEEE Trans. Microw. Theory Techn.*, vol. 64, no. 5, pp. 1667-1676, May 2016.
[26] S. Chen, M. Guo, K. Xu, P. Zhao, L. Dong and G. Wang, "A Frequency Synthesizer Based Microwave Permittivity Sensor Using CMRC Structure," *IEEE Access*, vol. 6, pp. 8556-8563, 2018.
[27] F. I. Jamal et al., "Low-Power Miniature K-Band Sensors for Dielectric Characterization of Biomaterials," *IEEE Trans. Microw. Theory Techn.*, vol. 65, no. 3, pp. 1012-1023, March 2017.
[28] J. -C. Chien, E. -C. Yeh, L. P. Lee, M. Anwar and A. M. Niknejad, "A microwave reconfigurable dielectric-based glucose sensor with 20 mg/dL sensitivity at sub-nL sensing volume in CMOS," 2015 *IEEE MTT-S Int. Microw. Symp. Dig*., Phoenix, AZ, USA, 2015, pp. 1-4.
[29] M. Abdolrazzaghi and M. Daneshmand, "Exploiting Sensitivity Enhancement in Micro-wave Planar Sensors Using Intermodulation Products With Phase Noise Analysis," *IEEE Transactions on Circuits and Systems I: Regular Papers*, vol. 67, no. 12, pp. 4382-4395, Dec. 2020.
[30] V. Ardila, F. Ramírez, A. Suárez, "Analytical and Numerical Bifurcation Analysis of Circuits Based on Nonlinear Resonators," *IEEE Trans. Microw. Theory Techn*., vol. 69, no. 10, pp. 4392-4405, Oct., 2021.
[31] Keysight, Advanced Design System.
[32] S. Hernández, M. Pontón and A. Suárez, "Simulation Method for Complex Multivalued Curves in Injection-Locked Oscillators," *IEEE Trans. Microw. Theory Techn.*, vol. 65, no. 11, pp. 4046-4062, Nov. 2017.
[33] M. A. Couker and L. J. Kushner, "A microstrip phase-trim device using a dielectric overlay," *IEEE Trans. Microw. Theory Techn*, vol. 42, no. 11, pp. 2023-2026, Nov. 1994.
[34] R.B. Keam, W.S. Holmes, "Uncertainty analysis of measurement of complex dielectric permittivity using microstrip transmission line", *Proc. SBMO/IEEE MTT-S Int. Microw. Optoelectron. Conf*., vol.1, pp.137-142 vol.1, 1995.
[35] I. J. Bahl and D. K. Trivedi, "A Designer's Guide to Microstrip Line," *Microwaves*, May 1977, pp. 174-182.
[36] F. Ramirez, M. Ponton, S. Sancho and A. Suarez, "Stability Analysis of Oscillation Modes in Quadruple-Push and Rucker's Oscillators," *IEEE Trans. Microw. Theory Techn.*, vol. 56, no. 11, pp. 2648-2661, Nov. 2008.
[37] A. Suarez, "Check the Stability: Stability Analysis Methods for Microwave Circuits," *IEEE Microw. Mag*., vol. 16, no. 5, pp. 69-90, June 2015.
[38] F. Ramirez, J. L. Garcia H, T. Fernandez and A. Suarez, "Nonlinear simulation techniques for the optimized design of push-push oscillators," *IEEE MTT-S Int. Microw. Symp. Dig*., Philadelphia, PA, USA, 2003, pp. 2157-2160.
[39] A. Suarez and F. Ramirez, "Analysis of stabilization circuits for phase-noise reduction in microwave oscillators," *IEEE Trans. Microw. Theory Techn*, vol. 53, no. 9, pp. 2743-2751, Sept. 2005.
[40] J. de Cos, A. Suárez and J. A. García, "Hysteresis and Oscillation in High-Efficiency Power Amplifiers," *IEEE Trans. Microw. Theory Techn*., vol. 63, no. 12, pp. 4284-4296, Dec. 2015
[41] H. Kawakami, "Bifurcation of periodic responses in forced dynamic nonlinear circuits: Computation of bifurcation values of the system parameters," *IEEE Trans Circ Syst*. vol. 31, no. 3, pp. 248-260, Mar., 1984.
[42] V. Rizzoli and A. Neri, "State of the art and present trends in nonlinear microwave CAD techniques," *IEEE Trans. Microwave Theory Techn*., vol. 36, no. 2, pp. 343–356, Feb., 1988.
[43] N. Ayllon, J. M. Collantes, A. Anakabe, I. Lizarraga, S. Soubercaze-Pun, S. Forestier, "Systematic approach to the stabilization of multitransistor circuits", *IEEE Trans. Microw. Theory Techn.*, vol. 59, no. 8, pp. 2073–2082, Aug. 2011.
[44] R. Quéré, E. Ngoya, M. Camiade, A. Suarez, M. Hessane and J. Obregon, "Large signal design of broadband monolithic microwave frequency dividers and phase-locked oscillators," *IEEE Trans. Microw. Theory Techn*., vol. 41, no. 11, pp. 1928–1938, Nov. 1993.
[45] A. Suárez, *Analysis and design of autonomous microwave circuits*, IEEE-Wiley, Jan. 2009.
[46] K. Kurokawa, "Some basic characteristics of broadband negative resistance oscillators", *Bell Syst. Tech. J*., vol. 48, pp. 1937–1955, 1969.
[47] F. Ramirez, M. Ponton, S. Sancho and A. Suarez, "Phase-Noise Analysis of Injection-Locked Oscillators and Analog Frequency Dividers," *IEEE Trans. Microw. Theory Techn.*, vol. 56, no. 2, pp. 393-407, Feb. 2008.
[48] J. C. Nallatamby, M. Prigent, J. C. Sarkissian, R. Quéré and J. Obregón, "A new approach to nonlinear analysis of noise behavior of synchronized oscillators and analog-frequency dividers," *IEEE Trans. Microw. Theory Techn.*, vol. 46, no. 8, pp. 1168–1171, Aug. 1998.
[49] J. M. Paillot, J. C. Nallatamby, M. Hessane, R. Quéré, M. Prigent and J. Rousset, "A general program for steady state, stability, and FM noise analysis of microwave oscillators," *IEEE MTT-S Int. Microw. Symp. Dig*., Dallas, Texas, USA, 1990, pp. 1287–1290.

Mabel Pontón (S'08–M'11) was born in Santander, Spain. She received the bachelor's degree in Telecommunication Engineering, master's degree in Information Technologies and Wireless Communications Systems, and Ph.D. degree from the University of Cantabria, Santander, Spain, in 2004, 2008, and 2010, respectively. In 2006, she joined the Communications Engineering Department of the University of Cantabria, Spain.

From 2011 to 2013, she was with the Group of Electronic Design and Applications, Georgia Institute of Technology, Atlanta, GA, USA, as a Post-Doctoral Research Fellow.

Her current research interests include the nonlinear analysis and simulation of radiofrequency and microwave circuits, with an emphasis on phase-noise, stability, and bifurcation analysis of complex oscillator topologies.

Sergio Sancho (A'04–M'04) received the degree in Physics from Basque Country University in 1997. In 1998 he joined the Communications Engineering Department of the University of Cantabria, Spain, where he received the Ph.D. degree in Electronic Engineering in February 2002. At present, he works at the University of Cantabria, as an Associate Professor of its Communications Engineering Department. His research interests include the nonlinear analysis of microwave autonomous circuits and frequency synthesizers, including stochastic and phase-noise analysis.

Amparo Herrera was born in Asturias (Spain) in 1963. She received the degree in Electronic Physics from the University of Cantabria (Spain) in June 1987, and the Ph.D degree from the same University in June 1995. In 1987 she joined the CIDA (Centro de Investigación y Desarrollo de la Armada) the Research and Development Spanish Army Centre, working on developing a RF&Microwave laboratory up to 1990 when she joined the Electronics Department of the

University of Cantabria, working on MMIC design. From 1992 to 1995, she collaborated with the Laboratory Philips Microwave Limeil (actually OMMIC), as result of this collaboration she presents her thesis receiving the Ph.D. degree in Electronics from the University of Cantabria in June 1995 in this work she had designed a high efficiency power amplifier for DECT and DCS applications a work for the Philips Microwave Limeill foundry (now called OMMIC). From 1995 she has been an associate professor at the University of Cantabria, and a member of its Communications Engineering Department. Her areas of interest include the MMIC and Hybrid design of microwave circuits and, specially, the power and low noise amplifier design and characterization. She has taken part as Main researcher in a big number of Spanish and European projects both of the III, IV, V and VI Frameworks and Spanish National R&D Plan. Also she has participated in a number of industrial projects with European and Spanish industries. Currently she is working in the design and development of MMIC devices on Si-Ge, GaN PHEMT technologies.

Almudena Suárez (M'96–SM'01–F'12) was born in Santander, Spain. She received the Licentiate degree in Electronic Physics and the Ph.D. degree from the University of Cantabria, Santander, Spain, in 1987 and 1992, respectively, and the Ph.D. degree in Electronics from the University of Limoges, France, in 1993. She is currently a full professor at University of Cantabria (Spain) and head of the research group Microwave Engineering and Radiocommunication Systems. She is a Fellow member of the IEEE (For applications of stability analysis to the computer aided design of microwave circuits) since 2012. She was an IEEE Distinguished Microwave Lecturer in 2006-2008. She has authored the book 'Analysis and design of autonomous microwave circuits' (IEEE-Wiley, 2009) and co-authored the book 'Stability Analysis of nonlinear microwave circuits' (Artech House, 2003). She is a member of the TPCs of IEEE International Microwave Symposium and European Microwave Week. She was a member of the Board of Directors of European Microwave Association (EuMA) from 2012 to 2020. She is the Publication Officer of EuMA since 2021. She received the Research Award of the Social Council of the University of Cantabria in 2021. She was the coordinator of the Communications and Electronic Technology Area for the Spanish National Evaluation and Foresight Agency (ANEP) between 2009 and 2013. She was the chair of the 2014 and 2015 editions of IEEE Topical Conference on RF/Microwave Power Amplifiers (PAWR), in Newport Beach and San Diego. She was the General TPC Chair of EuMW 2018. Prof. Suárez was the Editor-in-Chief of the International Journal of Microwave and Wireless Technologies from Cambridge University Press journals from 2013 to 2018 and is currently an Associate Editor for IEEE Microwave Magazine and IEEE Trans. Microw. Theory Techn. She has been the Chair of the IEEE Subcommittee for the Best paper Award in IEEE Microwave Magazine since 2017.